Journal of Materials Science: Materials in Electronics (2018) 29:11936–11944
https://doi.org/10.1007/s10854-018-9295-6

Carbon modified porous γ-Fe_2O_3 as anode for high performance Li-ion batteries

Chaoyu Duan[1] · Yanshuang Meng[1,3] · Mengqi Du[1] · Lei Wang[1] · Yue Zhang[2]

Received: 2 March 2018 / Accepted: 12 May 2018 / Published online: 17 May 2018

Abstract
Carbon modified porous γ-Fe_2O_3 particles (PFe_2O_3–C) are synthesized by a high temperature calcination method using sodium chloride as a template. During the nucleation and carbonation process, the $Fe(NO_3)_3$–$C_{10}H_{15}N_5$ complex uniformly dispersed on the surface of NaCl particles which can limit its longitudinal growth, thus forming independent and homogeneous nanoparticles with a diameter of about 30 nm. Because of this special structure, the γ-Fe_2O_3 particles have a sufficient interspace between them, which can not only provide a large number of active sites for storing lithium ions, but also shorten diffusion length for lithium ion transport. The introduction of carbon can offer additional lithium ion storage and improve overall electrical conductivity. This PFe_2O_3–C electrode exhibits excellent rate performance (1139, 1067, and 972 mAh g^{-1} at 2, 5, and 10 C, respectively, 1 C = 924 mAh g^{-1}) and cycle performance (up to 2100 mAh g^{-1} after 200 cycles at 0.3 C).

1 Introduction

Lithium-ion batteries (LIBs) play an important role in energy storage devices due to their extraordinary properties, such as long cycle life, high work voltage, no memory effect and environment-friendliness [1–3]. However, energy density and power density of LIBs still cannot satisfy the ever-increasing demands of electric vehicles and portable electronics [4, 5]. In principle, the energy storage is mainly achieved through the reversible conversion reaction in the electrode materials, which is the key factor to determine the performance of LIBs [2]. Therefore, exploring new anode materials to replace commercial graphite anode, which exhibits low theoretical capacity of 372 mAh g^{-1}, has aroused great concern [6].

In recent years, transition metal oxides (TMOs) gain increasing interest because of their high theoretical capacity (450–1500 mAh g^{-1}) and high abundance [3, 7]. Among these materials, Fe_2O_3 attracts more attentions due to its extraordinary properties, including high theoretical capacity (1007 mAh g^{-1}), low cost, non-toxicity, high corrosion resistance and easy to exploit [8–11]. Unfortunately, due to its poor intrinsic electronic conductivity and huge volume variation during the repeated lithiation/delithiation process, Fe_2O_3 electrode has high irreversible capacity loss, low initial coulombic efficiency and cycling stability, which has been hindering its commercial applications in LIBs [9, 12].

To overcome these drawbacks, many approaches have been exploited and could be classified into two groups. One of them is the construction of a porous architecture,which can not only withstand large volume changes caused by Li^+ insertion/extraction but also provide more active sites for storing lithium ions and effective paths for transferring lithium ion and electron [13–17]. Another one is the surface modification of TMOS nanostructure with carbonaceous materials to improve electrical conductivity as well as provide additional capacity [3, 8, 18–21]. Carbonaceous materials formed from different carbon precursors have different structural and electrochemical properties. Among these carbon precursors, ionic liquids (ILs) are gaining more and more attention because of their outstanding characteristics such as low viscosity, good fluidity, low vapor pressure and good thermal stability. Therefore, carbonaceous materials derived from ILs have a higher electrical conductivity and bonding strength [22].

✉ Yanshuang Meng
mengyanshuang@163.com

✉ Yue Zhang
yue.zhang@tamuk.edu

[1] School of Materials Science and Engineering, Lanzhou University of Technology, Lanzhou 730050, China

[2] Department of Mechanical and Industrial Engineering, Texas A&M University-Kingsville, Kingsville, TX 78363, USA

[3] State Key Laboratory of Advanced Processing and Recycling of Non-ferrous Metals, Lanzhou 730050, China

In this work, we used sodium chloride as a template to synthesize PFe_2O_3–C at high temperatures. The produced PFe_2O_3–C is consisted of independent and homogeneous γ-Fe_2O_3 nanoparticles with a diameter of ~ 30 nm. When served as an anode material for LIBs, PFe_2O_3–C exhibits high specific capacity and remarkable rate capability. It was also found that the increase of capacity is mainly occurred below 0.61 V due to the growth of polymeric gel-like film.

2 Experimental section

2.1 Synthesis of PFe_2O_3–C

The reagents were obtained from commercial suppliers and used without further purification. In a typical process, $Fe(NO_3)_3{\cdot}9H_2O$ (1.81 g), 1-butyl-3-methylimidazolium dicyanamide ([BMIm][$N(CN)_2$]) (1.28 g), and NaCl (18 g) were first dissolved in 35 mL deionized water. The solution was then dried in a drying oven at 80 °C for 24 h. After that, the obtained materials were annealed at 760 °C for 2 h in a tube furnace in flowing argon atmosphere to obtain carbon-modified Fe nanoparticles coated on the NaCl particles (Fe–C@NaCl). In the second step, the Fe–C@NaCl nanoparticles were heated at 260 °C for 6 h in air to oxidize the Fe to yield carbon-modified γ-Fe_2O_3 nanoparticles coated on the NaCl particles (PFe_2O_3–C@NaCl). After cooling to room temperature, the obtained powder was washed with deionized water to dissolve the NaCl and PFe_2O_3–C was obtained. For comparison, Fe_2O_3–C composites were also synthesized by carbonizing the mixture of $Fe(NO_3)_3{\cdot}9H_2O$ and [BMIm][$N(CN)_2$] without NaCl under the same conditions.

2.2 Structural and morphology characterization

The X-ray powder diffraction (XRD) patterns of PFe_2O_3–C@NaCl, PFe_2O_3–C and Fe_2O_3–C were collected by using a Rigaku D/max-2500 with Cu Kα radiation. Transmission electron microscopy (TEM) characterizations were carried out with a JEOL JEM-2010F equipment. The morphologies of PFe_2O_3–C@NaCl, PFe_2O_3–C and Fe_2O_3–C were observed on field emission scanning electron microscope (FESEM) by using an acceleration voltage of 15 kV (tescan MIRA3). Raman spectra of the samples were recorded on LabRAM-HR800. Nitrogen adsorption and desorption isotherms was performed on Quadrasorb SI. The surface area and pore size distribution of samples were calculated by BET and DJH method, respectively. The total pore volume was calculated by the adsorption amount of nitrogen at relative pressure (P/P_0) of 0.99.

2.3 Electrochemical measurement

The electrochemical measurements of the anode materials were carried out in a half coin-type cell. The coating slurry is prepared by mixing 70 wt% active material, 20 wt% Super P, and 10 wt% polyvinylidene fluoride in *N*-methyl pyrrolidone. The solvent was evaporated on a copper foil at 80 °C for 12 h. A lithium foil servedas counter electrode and was separated from the work electrode with the Celgard 2400 micro-porous polypropylene film. The electrolyte is a solution of 1 M lithium hexafluorophosphate (LiPF6) that dissolved in the mixture of ethylene carbonate (EC) and 1,2-dimethoxyethane (DME) with a volume ratio of 1:1. The cycle performance and rate capability were performed in the voltage range between 0.001 and 3.0 V (vs. Li/Li^+) on a battery test system (LAND CT2001, China). Electrochemical impedance spectra (EIS) and cyclic voltammetry (CV) measurements were performed at room temperature on a CHI660D electrochemistry workstation (Chenhua, China).

3 Result and discussion

Figure 1 shows the XRD patterns of PFe_2O_3–C@NaCl, PFe_2O_3–C and Fe_2O_3–C. For PFe_2O_3–C@NaCl samples, the diffraction peaks at 27.3°, 31.6°, 45.3°, 53.7°, 56.3°, 66.1°, 72.92°, 75.1° and 83.8° are assigned to (111), (200), (220), (311), (222), (400), (331), (420) and (422) planes of NaCl (JCPDS No 70-2509), respectively. The diffraction peak of γ-Fe_2O_3 was less obvious, which may be attributed to the low content of γ-Fe_2O_3 in PFe_2O_3–C@NaCl [23]. For PFe_2O_3–C and Fe_2O_3–C, all diffraction peaks well correspond to the planes of maghemite γ-Fe_2O_3 (JCPDS No 39-1346) [8, 24]. Sharp diffraction peaks indicate good crystallinity of both samples. No other diffraction peak was observed, indicating that no other polymorphs iron oxide generation [25]. From previous literature, it can be known that the γ-Fe_2O_3 will not be further oxidized during the cycle [26]. The diffraction peak of carbon was not observed, which may be due to the low content of carbon PFe_2O_3–C and Fe_2O_3–C. XRD results indicate that PFe_2O_3–C and Fe_2O_3–C materials were successfully prepared [27].

SEM and TEM are used to analyze the morphologies of PFe_2O_3–C@NaCl, PFe_2O_3–C and Fe_2O_3–C materials. From Fig. 2a–c, we can see that the PFe_2O_3–C uniformly dispersed on the surface of NaCl particles. The addition of NaCl can limit the longitudinal growth of the $Fe(NO_3)_3$–$C_{10}H_{15}N_5$ complex in nucleation and carbonation process, which result in independent and

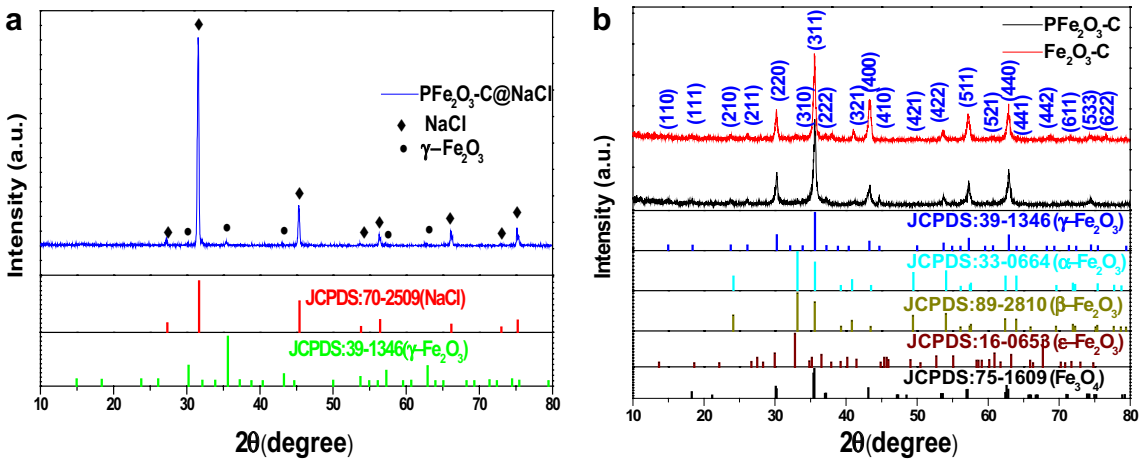

Fig. 1 XRD patterns of PFe_2O_3–C@NaCl (**a**), PFe_2O_3–C and Fe_2O_3–C (**b**)

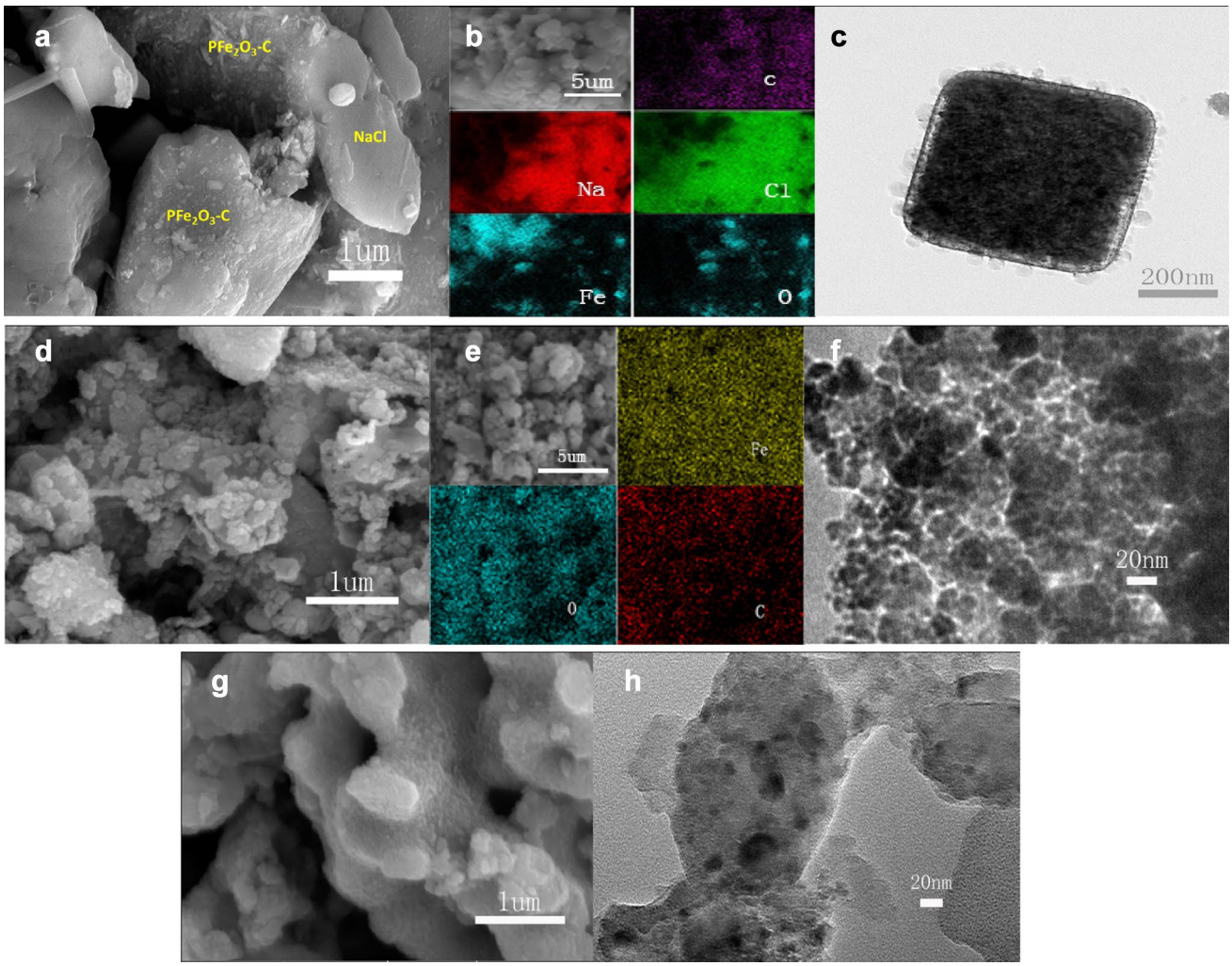

Fig. 2 **a** SEM image, **b** EDS elemental mapping, and **c** TEM image of PFe_2O_3–C@NaCl; **d** SEM image, **e** EDS elemental mapping, and **f** TEM image of PFe_2O_3–C; **g** SEM image and **h** TEM image of Fe_2O_3–C

homogeneous nanoparticles with a diameter of ~ 30 nm. As can be seen from Fig. 2d, PFe_2O_3–C material has rough surfaces and the nanoparticles have a diameter of about 30 nm. While the surface of Fe_2O_3–C is smooth and the Fe_2O_3 particles have a large diameter of ~ 500 nm (Fig. 2g, h). The result of EDS elemental analysis show the uniform distribution of carbon on the Fe_2O_3 particles, which can provide additional sites for lithium ion storage and improve the electrical conductivity (Fig. 2e). The TEM image (Fig. 2f) further confirms that PFe_2O_3–C consists of independent and homogeneous nanoparticles that are separated by significant gap. This unique structure can shorten the lithium-ion and electron transport path, buffer the lithium-ion volume expansion, and provide more active sites. In comparison, the Fe_2O_3–C material in Fig. 2g, h consists of bulk particles with no obvious boundaries between the particles. This structure cannot facilitate lithium ion transport or buffer the volume expansion [28].

To further study the structure of carbon in the PFe_2O_3–C and Fe_2O_3–C, the Raman spectroscopy was applied. In Fig. 3a, the two broad Raman bands at about 1342 and 1586 cm^{-1} correspond to the D-band of edge and disordered structures and the ordered sp^2-hybridized G-band, respectively [29]. The intensity ratio of D band to G band (I_D/I_G) is indicator of the crystallinity of various carbon materials. The larger value of I_D/I_G, the higher the degree of disorder in the carbon material [30]. The I_D/I_G ratios of PFe_2O_3–C and Fe_2O_3–C were 1.22 and 1.13, respectively, indicating that PFe_2O_3–C has more defects and lower ordered structure, which can provide more active sites for lithium ion storage, thus contributing extra specific capacity. Three large bands at 700 cm^{-1} (A1), 500 cm^{-1} (E) and 350 cm^{-1} (T1) attributed to the vibration modes of γ-Fe_2O_3, further confirming that Fe element was completely oxidized to γ-Fe_2O_3 [31].

N_2 adsorption–desorption isotherms of PFe_2O_3–C and Fe_2O_3–C are shown in Fig. 3b. The isothermal curves of both samples exhibit a type IV curve with H3 hysteresis loop located at a relative pressure of 0.4–1.0. The pore size distribution (inset in Fig. 3b) indicates that PFe_2O_3–C has more micropores and mesopores [32, 33]. The specific surface area of PFe_2O_3–C (26.9 $m^2\ g^{-1}$) is about four times of Fe_2O_3–C (6.7 $m^2\ g^{-1}$), which can provide more active sites for the storage of lithium ions and serve as an effective electron transport path [34]. The pore volume of PFe_2O_3–C (about 0.072 $cm^3\ g^{-1}$) is also much larger than Fe_2O_3–C (about 0.021 $cm^3\ g^{-1}$). Therefore, PFe_2O_3–C has better performance on buffering the volume change of the Fe_2O_3 nanocrystal during charge/discharge cycles. This is consistent with the results of TEM and SEM.

Figure 4a shows the CV plots of PFe_2O_3–C electrode for four cycles at a scan rate of 0.1 mV s^{-1} from 0 to 3.0 V (vs. Li/Li^+). These plots display a typical pattern of Fe_2O_3–C composite [35, 36]. The electrochemical reaction of Li^+ with Fe_2O_3 can be described by the following equations [37–40]:

$$Fe_2O_3 + xLi^+ + xe^- \rightarrow Li_xFe_2O_3 \quad (1)$$

$$Li_2Fe_2O_3 + 4Li^+ + 4e^- \rightarrow 2Fe + 3Li_2O \quad (2)$$

$$2Fe + 3Li_2O \leftrightarrow Fe_2O_3 + 6Li^+ + 6e^- \quad (3)$$

$$Li_xFe_2O_3 + (2 - x)Li^+ + (2 - x)e^- \rightarrow Li_2Fe_2O_3 \quad (4)$$

$$Fe + Li_2O \rightarrow FeO + 2Li^+ + 2e^- \quad (5)$$

$$2FeO + Li_2O \rightarrow Fe_2O_3 + 2Li^+ + 2e^- \quad (6)$$

In the first cathode curve, the peak at 0.97 V is related to the lithium intercalation into the γ-Fe_2O_3 crystal structure (Eq. 1). The capacity associated with the voltage drop is 267 mAh g^{-1} (Fig. 4b), which is equivalent to the uptake of 1.6 mol of Li (x = 1.6, in Eq. 1) per mole of PFe_2O_3–C. Thus, the above steps generate the $Li_{1.6}Fe_2O_3$ intermediate product, indicating that the crystal structure of γ-Fe_2O_3

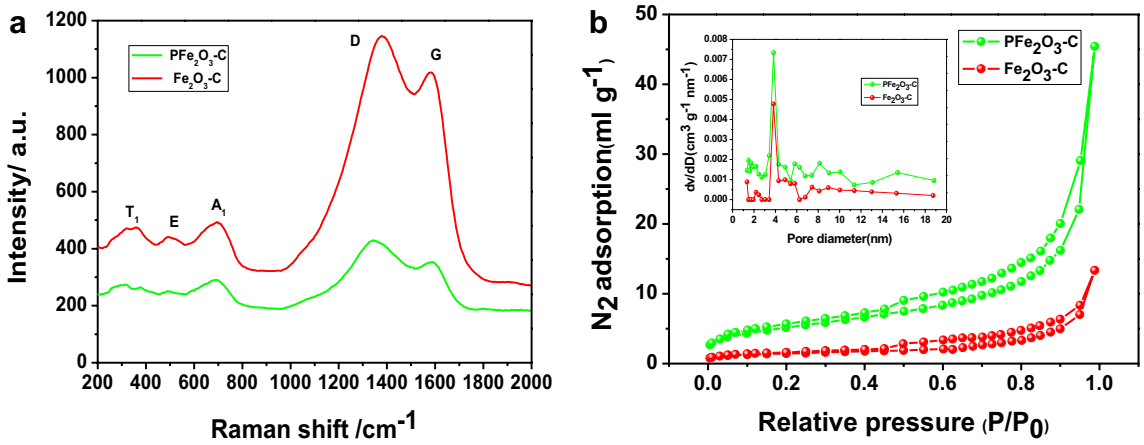

Fig. 3 **a** Raman spectra, **b** N_2 adsorption–desorption isotherms and the pore size distribution curves of PFe_2O_3–C and Fe_2O_3–C

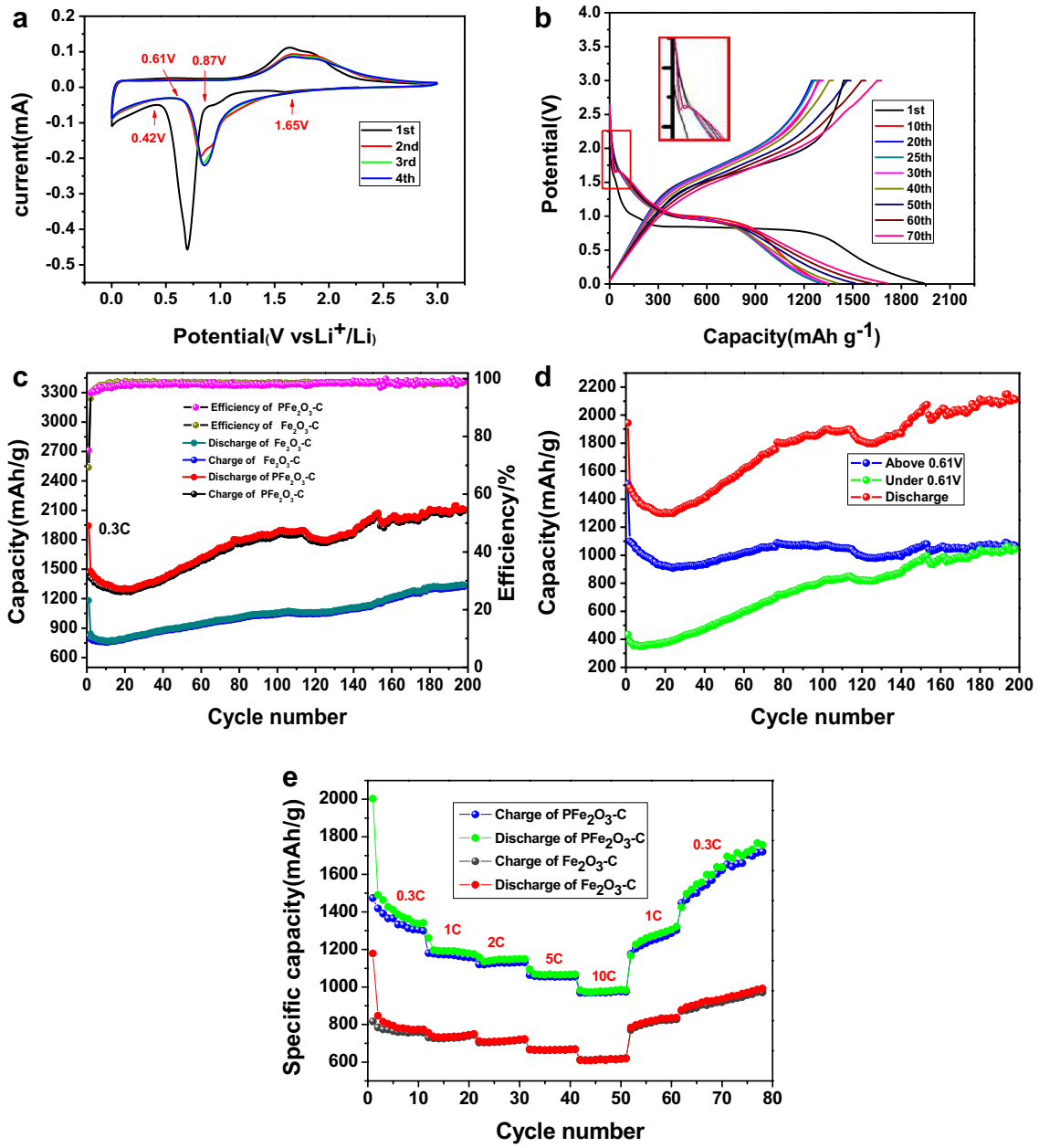

Fig. 4 **a** CV plot of PFe_2O_3–C, **b** voltage profiles of PFe_2O_3–C, **c** cycle performances of PFe_2O_3–C and Fe_2O_3–C at the current density of 0.3 C in 0.01–3.00 V, **d** schematic illustrations of two parts of battery capacity of PFe_2O_3–C at 0.3 C between 0.01 and 3 V, and **e** rate capability of PFe_2O_3–C and Fe_2O_3–C. (Color figure online)

is not destroyed [37]. The peak at 0.69 V results from the conversion of $Li_{1.6}Fe_2O_3$ to $Li_2Fe_2O_3$ (Eq. 4, consumed 2–x = 0.4 mol of Li^+), the reduction of Fe^{3+} to Fe^0 (Eq. 2, consumed 4 mol Li^+), and the formation of solid electrolyte interface (SEI) film. It is noteworthy that this peak is vanished at 0.42 V in the first cycle and 0.61 V in the following cycles. The capacity of 1508 mAh g^{-1} is achieved from the open circuit voltage (OCV) to the 0.42 V, representing a total uptake of 9 mol Li^+ per mole of PFe_2O_3–C, which corresponds to a complete reduction of Fe^{3+} to Fe^0 (including Eqs. 1, 2, 4) and SEI film. Obviously, 3 mol $Li^+$is consumed to form SEI via subtraction. The total discharge capacity in the first cycle finally reached 1943.8 mAh g^{-1}, which is equivalent to the uptake of 11.6 mol of Li^+. Therefore, the proportion of Li^+ to form SEI is 25.9%, which is in agreement with the initial coulombic efficiency of 75.2% from voltage profiles of PFe_2O_3–C in Fig. 4b. Another two anodic peaks at 1.63 and 1.83 V are attributed to the oxidation of Fe^0 to Fe^{2+} and Fe^{3+} (Eqs. 5, 6), respectively. In the subsequent cycles, the shift of the main cathode peak from 0.69 to

0.82 V derives from the small scale structural adjustment of PFe_2O_3–C, which enhances the electrical contact among the cell components [41]. Starting from the second cycle, the peak position and shape of the CV almost overlap, indicating that the electrode has great reversibility and integrity [42].

Figure 4b shows the voltage profiles of PFe_2O_3–C at the 1st, 10th, 20th, 25th, 30th, 40th, 50th, 60th, and 70th cycles at a current density of 0.3 C. The first discharge and charge capacity are 1943.8 and 1462.1 mAh g^{-1}, respectively. The irreversible capacity loss is due to the formation of SEI film and electrolyte decomposition, resulting in a coulombic efficiency of only 75.22% [43–45]. The discharge voltage plateau at 0.82 V in the first cycle is different from those of other cycles at 0.93 V, indicating that irreversible reactions occurred in the first cycle, which is consistent with the CV results. The discharge curves below 0.61 V become higher and more sloping with the increase of cycle number, indicating that the growth of PGF tended to be easier due to the nanocrystallization of the particles during the repeated lithiation/delithiation process. Interestingly, after 25 cycles, a slight plateau appears at 1.6 V, becoming more obvious as charge/discharge cycles increase, even forming a semicircle at 70 cycles. The main reason is that the stable PGF generated on the surface of the active substance increases the diffusion distance and the resistance of Li^+. Meanwhile, the charging curve is a sloping curve with no obvious voltage platform, owing to the large surface area induced during the former discharge process which could widen the reaction site energy range for intercalation compound or the amorphous character of the active materials itself.

Figure 4c shows the long cycling performance of PFe_2O_3–C and Fe_2O_3–C at a current density of 0.3 C. The reversible capacity of PFe_2O_3–C retains to 1306 mAh g^{-1} after 20 cycles and increases to 1881 mAh g^{-1} after 100 cycles. The capacity fading of PFe_2O_3–C electrode in the preliminary cycles is due to the decomposition of the SEI film on the Fe_2O_3-based anode surface. According to the SEM and BET results, the PFe_2O_3–C electrode has a larger specific surface area than Fe_2O_3–C, thus requiring ten more cycles to form the SEI film before terminating by insulate SEI. Subsequent increase in cycle capacity is due to the extra capacity resulting from the reversible formation/decomposition of the polymeric gel-like film (PGF) on the active material surface [46]. This phenomenon has also been found in Fe_3O_4 and many other nanostructured metal oxide anodes [47–50]. Due to the high specific surface area of PFe_2O_3–C, more PGF can be grown on the surface of the active material, leading to larger capacity increase of PFe_2O_3–C than Fe_2O_3–C.

To study the behavior of the discharge capacity (red curve) in each voltage range, the curves are split into two parts: above 0.61 V and below 0.61 V, as shown in Fig. 4d. The blue curve represents the capacity above 0.61 V and the green curve stands for the capacity below 0.61 V. The blue curve decreases gradually before 20 cycles, which is parallel to the red curve. After 20 cycles, the blue curve remains relatively stable. While the green curve increases after the 10th cycle, and then follows the trend of the red curve after 20 cycles. This indicates that the increased capacity mainly occurs in the region below 0.61 V, which is due to the PGF growth and the fast decomposition of electrolyte at low potentials [51].

In addition to excellent reversible capacity, PFe_2O_3–C also exhibits outstanding rate performance. As shown in Fig. 4e, the rate capacity test was measured on a duplicate cell at different current rates of 0.3, 1, 2, 5, and 10 C in the voltage range of 0.01–3.0 V. The average reversible capacity of PFe_2O_3–C electrode are 1427, 1193, 1139, 1067, and 972 mAh g^{-1} at 0.3, 1, 2, 5, and 10 C, respectively, which are significantly better than the Fe_2O_3–C electrode. The PFe_2O_3–C electrode still provides a higher reversible capacity of 972 mAh g^{-1} even at a high current density of 10 C, correponding to ~ 68.1% of the capacity at 0.3 C. When returning to 0.3 C, the reversible capacity of both samples increased in subsequent cycles, which is similar to the cycling performance in Fig. 4c.

The dynamic behavior of PFe_2O_3–C and Fe_2O_3–C was investigated by EIS, as shown in Fig. 5a. The semicircular diameter of PFe_2O_3–C is smaller than that of Fe_2O_3–C, indicating that the charge-transfer resistance of PFe_2O_3–C is small. To further study the PGF growth, the EIS of another duplicate at 10th, 20th, 30th, 40th, 50th, 84th and 99th cycles was measured at 1 C, as show in Fig. 5b. The impedance data is analyzed by fitting the equivalent circuit (inset of Fig. 5b), where R0, Rf, and Rd represent the electrolyte resistance, the surface film resistance, and the charge transfer resistance, respectively. Cf and Cd are the corresponding capacitances of Rf and Rd, respectively. Therefore, the electronic component groups of Part f (Rf, Cf) and Part d (Rd, Cd) are related to the SEI layer and PGF, respectively. The fitted result for charge transfer resistance (Rd) is shown in Table 1. The value of Rd decreased in the first 30 cycles and increased in subsequent cycles, which is consistent with the capacity behavior. This is due to that a small amount of PGF is generated before the first 30 cycles and more PGF is grown after 30 cycles during charge–discharge process, thereby consuming more Li^+. This result further explains why the voltage platform appears at ~ 1.6 V (Fig. 4b).

4 Conclusions

PFe_2O_3–C particles were synthesized by using sodium chloride as a templating agent. Compared with Fe_2O_3–C, PFe_2O_3–C consists of uniform and independent Fe_2O_3 nanoparticles with a diameter of about 30 nm, delivering

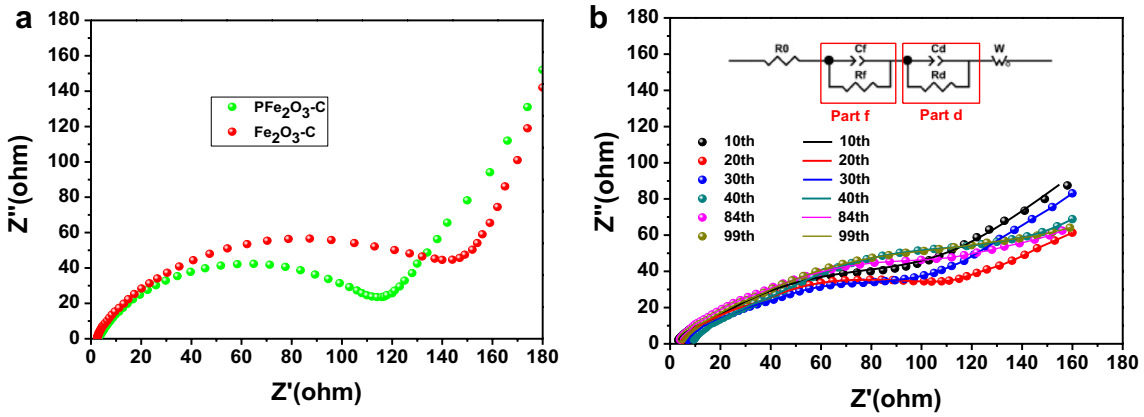

Fig. 5 **a** EIS of PFe_2O_3–C and Fe_2O_3–C before CV. **b** Nyquist plots of PFe_2O_3–C at fully charge stage upon cycles (equivalent electrical circuit in inset)

Table 1 The parameters obtained by fitting an equivalent circuit of PFe_2O_3–C electrodes

Cycle number	10	20	30	40	84	99
Rd (Ω)	78.9	74.2	66.8	86.2	104.2	124.9

high rate capability and cycling performance. This can be attributed porous structure of PFe_2O_3–C, which can provide sufficient active sites for storing lithium ions, shorten the diffusion length and buffer the volume expansion. In addition, integration of carbon can also offer additional lithium ion storage and improve the electrical conductivity of the material. These results indicate this method can be applied to prepare electrode materials for highly efficient energy storage applications, which with further optimization should be suitable for widespread applications.

Acknowledgements The authors thank the National Natural Science Foundation of China (NFSC) (Grant Nos. 51364024, 51404124) and the Foundation for Innovation Groups of Basic Research in Gansu Province (No. 1606RJIA322).

References

1. M. Chen, J. Liu, D. Chao, J. Wang, J. Yin, J. Lin, H. Jin Fan, Z. Xiang Shen, Porous α-Fe_2O_3 nanorods supported on carbon nanotubes-graphene foam as superior anode for lithium ion batteries. Nano Energy **9**(9), 364–372 (2014). https://doi.org/10.1016/j.nanoen.2014.08.011
2. N. Zhang, C. Chen, X. Yan, Y. Huang, J. Li, J. Ma, D.H.L. Ng, Bacteria-inspired fabrication of Fe_3O_4-carbon/graphene foam for lithium-ion battery anodes. Electrochim. Acta **223**, 39–46 (2017). https://doi.org/10.1016/j.electacta.2016.12.006
3. M. Liu, H. Jin, E. Uchaker, Z. Xie, Y. Wang, G. Cao, S. Hou, J. Li, One-pot synthesis of in-situ carbon-coated Fe_3O_4 as a long-life lithium-ion battery anode. Nanotechnology **28**(15), 155603 (2017). https://doi.org/10.1088/1361-6528/aa6143
4. L. Yang, G.N. Guo, H.J. Sun, X.D. Shen, J.H. Hu, A.G. Dong, D. Yang, Ionic liquid as the C and N sources to prepare yolk-shell Fe_3O_4@N-doped carbon nanoparticles and its high performance in lithium-ion battery. Electrochim. Acta **190**, 797–803 (2016). https://doi.org/10.1016/j.electacta.2016.01.028
5. X. Fan, S. Li, H. Zhou, L. Lu, One-pot high temperature hydrothermal synthesis of Fe_3O_4@C/graphene nanocomposite as anode for high rate lithium ion battery. Electrochim. Acta **180**, 1041–1049 (2015). https://doi.org/10.1016/j.electacta.2015.09.048
6. Y. Wang, J. Han, X. Gu, S. Dimitrijev, Y. Hou, S. Zhang, Ultrathin Fe_2O_3 nanoflakes using smart chemical stripping for high performance lithium storage. J Mater Chem A **5**(35), 18737–18743 (2017). https://doi.org/10.1039/c7ta05798a
7. Y. Dong, K.C. Yung, R. Ma, X. Yang, Y.-S. Chui, J.-M. Lee, J.A. Zapien, Graphene/acid assisted facile synthesis of structure-tuned Fe_3O_4 and graphene composites as anode materials for lithium ion batteries. Carbon **86**, 310–317 (2015). https://doi.org/10.1016/j.carbon.2015.01.062
8. J. Hu, W. Li, C. Liu, H. Tang, T. Liu, H. Guo, X. Song, J. Zheng, Y. Liu, Y. Duan, F. Pan, The formation and mechanism of nano-monocrystalline γ-$Fe_2O_3$with graphene-shell for high-performance lithium ion batteries. RSC Adv. **6**(57), 51777–51782 (2016). https://doi.org/10.1039/c6ra08143f
9. F. Wu, R. Huang, D. Mu, B. Wu, Y. Chen, Controlled synthesis of graphitic carbon-encapsulated α-Fe_2O_3 nanocomposite via low-temperature catalytic graphitization of biomass and its lithium storage property. Electrochim. Acta **187**, 508–516 (2016). https://doi.org/10.1016/j.electacta.2015.11.108
10. P. Santhoshkumar, K. Prasanna, Y.N. Jo, I.N. Sivagami, S.H. Kang, C.W. Lee, A facile and highly efficient short-time homogenization hydrothermal approach for the smart production of high-quality α-Fe_2O_3 for rechargeable lithium batteries. J Mater Chem A **5**(32), 16712–16721 (2017). https://doi.org/10.1039/c7ta04797e
11. Y. Wang, J. Guo, L. Li, Y. Ge, B. Li, Y. Zhang, Y. Shang, A. Cao, High-loading Fe_2O_3/SWNT composite films for

lithium-ion battery applications. Nanotechnology **28**(34), 345703 (2017). https://doi.org/10.1088/1361-6528/aa7a81
12. Y. Liu, X. Wang, W. Ma, J. Mujtaba, G. Sun, J. Zhao, H. Sun, One-pot hydrothermal synthesis of hollow Fe_3O_4 microspheres assembled with nanoparticles for lithium-ion battery anodes. Mater. Lett. **172**, 76–80 (2016). https://doi.org/10.1016/j.matlet.2016.01.157
13. S. Chen, R. Zhou, Y. Chen, Y. Fu, P. Li, Y. Song, L. Wang, Carbon-covered Fe_3O_4 hollow cubic hierarchical porous composite as the anode material for lithium-ion batteries. J. Nanopart. Res. **19**(4), 127 (2017). https://doi.org/10.1007/s11051-017-3794-x
14. G. Liu, J. Shao, Y. Gao, Z. Chen, Q. Qu, Green fabrication of sandwich-like and dodecahedral C@Fe_3O_4@C as high-performance anode for lithium-ion batteries. J. Solid State Electrochem. **21**(9), 1–8 (2017). https://doi.org/10.1007/s10008-017-3667-3
15. M.-S. Wu, M.-J. Wang, J.-J. Jow, Fabrication of porous nickel oxide film with open macropores by electrophoresis and electrodeposition for electrochemical capacitors. J. Power Sources **195**(12), 3950–3955 (2010). https://doi.org/10.1016/j.jpowsour.2009.12.136
16. T.-T. Yang, W.-K. Zhu, W.-L. Liu, F.-G. Kong, M.-M. Ren, Q.-Z. Liu, Z.-Z. Yang, X.-Q. Wang, X.-L. Duan, Preparation of yolk–shell Fe_3O_4@N-doped carbon nanocomposite particles as anode in lithium ion batteries. J. Mater. Sci. Mater. Electron. **28**(16), 11569–11575 (2017). https://doi.org/10.1007/s10854-017-6957-8
17. M. Sun, M. Sun, H. Yang, W. Song, Y. Nie, S. Sun, Porous Fe_2O_3 nanotubes as advanced anode for high performance lithium ion batteries. Ceram. Int. **43**(1), 363–367 (2017). https://doi.org/10.1016/j.ceramint.2016.09.166
18. C. Ma, J. Shi, Y. Zhao, N. Song, Y. Wang, A novel porous reduced microcrystalline graphene oxide supported Fe_3O_4@C nanoparticle composite as anode material with excellent lithium storage performances. Chem. Eng. J. **326**, 507–517 (2017). https://doi.org/10.1016/j.cej.2017.05.180
19. H. Luo, D. Ji, Z. Yang, Y. Huang, G. Xiong, Y. Zhu, R. Guo, Y. Wan, An ultralight and highly compressible anode for Li-ion batteries constructed from nitrogen-doped carbon enwrapped Fe_3O_4 nanoparticles confined in a porous 3D nitrogen-doped graphene network. Chem. Eng. J. **326**, 151–161 (2017). https://doi.org/10.1016/j.cej.2017.05.102
20. Y. Li, C. Zhu, T. Lu, Z. Guo, D. Zhang, J. Ma, S. Zhu, Simple fabrication of a Fe_2O_3/carbon composite for use in a high-performance lithium ion battery. Carbon **52**, 565–573 (2013). https://doi.org/10.1016/j.carbon.2012.10.015
21. T.-A. Nguyen, S.-W. Lee, Green synthesis of N-doped carbon modified iron oxides (N-Fe_2O_3@carbon) using sustainable gelatin cross-linker for high performance Li-ion batteries. Electrochim. Acta **248**, 37–45 (2017). https://doi.org/10.1016/j.electacta.2017.07.114
22. G. Wang, Y. Meng, L. Wang, J. Xia, F. Zhu, Y. Zhang, Yolk-shell Co_3O_4-CoO/carbon composites for lithium-ion batteries with enhanced electrochemical properties. Int. J. Electrochem. Sci. **12**, 2618–2627 (2017). https://doi.org/10.20964/2017.04.73
23. O. Font, N. Moreno, X. Querol, M. Izquierdo, E. Alvarez, S. Diez, J. Elvira, D. Antenucci, H. Nugteren, F. Plana, A. López, P. Coca, F.G. Peña, X-ray powder diffraction-based method for the determination of the glass content and mineralogy of coal (co)-combustion fly ashes. Fuel **89**(10), 2971–2976 (2010). https://doi.org/10.1016/j.fuel.2009.11.024
24. J. Hu, J. Zheng, L. Tian, Y. Duan, L. Lin, S. Cui, H. Peng, T. Liu, H. Guo, X. Wang, F. Pan, A core-shell nanohollow-gamma-Fe_2O_3@graphene hybrid prepared through the Kirkendall process as a high performance anode material for lithium ion batteries. Chem. Commun. **51**(37), 7855–7858 (2015). https://doi.org/10.1039/c5cc01195g
25. T. Song, P. Zhang, J. Zeng, T. Wang, A. Ali, H. Zeng, Boosting the photocatalytic H_2 evolution activity of Fe_2O_3 polymorphs (α-, γ- and β-Fe_2O_3) by fullerene [C_{60}]-modification and dye-sensitization under visible light irradiation. RSC Adv. **7**(46), 29184–29192 (2017). https://doi.org/10.1039/c7ra03451b
26. X. Lv, J. Deng, B. Wang, J. Zhong, T.-K. Sham, X. Sun, X. Sun, γ-Fe_2O_3@CNTs anode materials for lithium ion batteries investigated by electron energy loss spectroscopy. Chem. Mater. **29**(8), 3499–3506 (2017). https://doi.org/10.1021/acs.chemmater.6b05356
27. L. Guo, Y. Ding, C. Qin, W. Li, J. Du, Z. Fu, W. Song, F. Wang, Nitrogen-doped porous carbon spheres anchored with Co_3O_4 nanoparticles as high-performance anode materials for lithium-ion batteries. Electrochim. Acta **187**, 234–242 (2016). https://doi.org/10.1016/j.electacta.2015.11.065
28. J. Liu, X.W. Liu, Two-dimensional nanoarchitectures for lithium storage. Adv. Mater. **24**(30), 4097–4111 (2012). https://doi.org/10.1002/adma.201104993
29. Q. Guan, J. Cheng, B. Wang, W. Ni, G. Gu, X. Li, L. Huang, G. Yang, F. Nie, Needle-like Co_3O_4 anchored on the graphene with enhanced electrochemical performance for aqueous supercapacitors. ACS Appl. Mater. Interfaces **6**(10), 7626–7632 (2014). https://doi.org/10.1021/am5009369
30. X. Wang, Q. Weng, X. Liu, X. Wang, D.M. Tang, W. Tian, C. Zhang, W. Yi, D. Liu, Y. Bando, D. Golberg, Atomistic origins of high rate capability and capacity of N-doped graphene for lithium storage. Nano Lett. **14**(3), 1164–1171 (2014). https://doi.org/10.1021/nl4038592
31. Y. El Mendili, J.F. Bardeau, N. Randrianantoandro, J.M. Greneche, F. Grasset, Structural behavior of laser-irradiated gamma-Fe_2O_3 nanocrystals dispersed in porous silica matrix: gamma-Fe_2O_3 to alpha-Fe_2O_3 phase transition and formation of epsilon-Fe_2O_3. Sci. Technol. Adv. Mater. **17**(1), 597–609 (2016). https://doi.org/10.1080/14686996.2016.1222494
32. H. Jiang, W. Zhang, P. Chen, W. Zhang, G. Wang, X. Luo, S. Luo, Equipping an adsorbent with an indicator: a novel composite to simultaneously detect and remove heavy metals from water. J. Mater. Chem. A **4**(30), 11897–11907 (2016). https://doi.org/10.1039/c6ta04885d
33. S.H. Lee, S.H. Yu, J.E. Lee, A. Jin, D.J. Lee, N. Lee, H. Jo, K. Shin, T.Y. Ahn, Y.W. Kim, H. Choe, Y.E. Sung, T. Hyeon, Self-assembled Fe_3O_4 nanoparticle clusters as high-performance anodes for lithium ion batteries via geometric confinement. Nano Lett. **13**(9), 4249–4256 (2013). https://doi.org/10.1021/nl401952h
34. G. Zhou., D.-W. Wang, F. Li, L. Zhang., N. Li., Z.-S. Wu, L. Wen, H.-M. Lu, G.Q.M. Cheng, Graphene-wrapped Fe_3O_4 anode material with improved reversible capacity and cyclic stability for lithium ion batteries. Chem. Mater. **22**(18), 5306–5313 (2010). https://doi.org/10.1021/cm101532x
35. Y.-H. Sun, S. Liu, F.-C. Zhou, J.-M. Nan, Electrochemical performance and structure evolution of core-shell nano-ring α-Fe_2O_3@carbon anodes for lithium-ion batteries. Appl. Surf. Sci. **390**, 175–184 (2016). https://doi.org/10.1016/j.apsusc.2016.08.071
36. X. Lv, Y. Zhu, T. Yang, H. Zhang, X. Cui, H. Yue, D. Liu, J. Chen, J. Ji, Liquid-solid-solution assembly of morphology-controllable Fe_2O_3/graphene nanostructures as high-performance LIB anodes. Ceram. Int. **42**(16), 19006–19011 (2016). https://doi.org/10.1016/j.ceramint.2016.09.056
37. Y. Wu, P. Zhu, M.V. Reddy, B.V. Chowdari, S. Ramakrishna, Maghemite nanoparticles on electrospun CNFs template as prospective lithium-ion battery anode. ACS Appl. Mater. Interfaces **6**(3), 1951–1958 (2014). https://doi.org/10.1021/am404939q
38. D. Larcher, D. Bonnin, R. Cortes, I. Rivals, L. Personnaz, J.M. Tarascon, Combined XRD, EXAFS, and Mössbauer studies of the reduction by lithium of α-Fe_2O_3 with various particle

sizes. J. Electrochem. Soc. **150**(12), A1643 (2003). https://doi.org/10.1149/1.1622959
39. C.T. Cherian, J. Sundaramurthy, M. Kalaivani, P. Ragupathy, P.S. Kumar, V. Thavasi, M.V. Reddy, C.H. Sow, S.G. Mhaisalkar, S. Ramakrishna, B.V.R. Chowdari, Electrospun α-Fe_2O_3 nanorods as a stable, high capacity anode material for Li-ion batteries. J. Mater. Chem. **22**(24), 12198 (2012). https://doi.org/10.1039/c2jm31053h
40. Z. Wang, D. Luan, S. Madhavi, Y. Hu, X.W. Lou, Assembling carbon-coated α-Fe_2O_3 hollow nanohorns on the CNT backbone for superior lithium storage capability. Energy Environ. Sci. **5**, 5252–5256 (2012). https://doi.org/10.1039/c1ee02831f
41. M.V. Reddy, T. Yu, C.H. Sow, Z.X. Shen, C.T. Lim, G.V. Subba Rao, B.V.R. Chowdari, α-Fe_2O_3 nanoflakes as an anode material for li-ion batteries. Adv. Func. Mater. **17**(15), 2792–2799 (2007). https://doi.org/10.1002/adfm.200601186
42. X. Xing, R. Liu, S. Liu, S. Xiao, Y. Xu, C. Wang, D. Wu, Surfactant-assisted hydrothermal synthesis of cobalt oxide/nitrogen-doped graphene framework for enhanced anodic performance in lithium ion batteries. Electrochim. Acta **194**, 310–316 (2016). https://doi.org/10.1016/j.electacta.2016.02.096
43. T. Muraliganth, A. Vadivel Murugan, A. Manthiram, Facile synthesis of carbon-decorated single-crystalline Fe_3O_4 nanowires and their application as high performance anode in lithium ion batteries. Chem. Commun. **47**, 7360–7362 (2009). https://doi.org/10.1039/b916376j
44. S.M. Yuan, J.X. Li, L.T. Yang, L.W. Su, L. Liu, Z. Zhou, Preparation and lithium storage performances of mesoporous Fe_3O_4@C microcapsules. ACS Appl. Mater. Interfaces **3**(3), 705–709 (2011). https://doi.org/10.1021/am1010095
45. T. Zhu, J.S. Chen, X.W. Lou, Glucose-assisted one-pot synthesis of FeOOH nanorods and their transformation to Fe_3O_4@carbon nanorods for application in lithium ion batteries. J. Phys. Chem. C **115**(19), 9814–9820 (2011). https://doi.org/10.1021/jp2013754
46. X. Huang, J. Chen, Z. Lu, H. Yu, Q. Yan, H.H. Hng, Carbon inverse opal entrapped with electrode active nanoparticles as high-performance anode for lithium-ion batteries. Sci. Rep. **3**, 2317 (2013). https://doi.org/10.1038/srep02317
47. F. Zheng, Z. Yin, H. Xia, Y. Zhang, MOF-derived porous Co_3O_4 cuboids with excellent performance as anode materials for lithium-ion batteries. Mater. Lett. **197**, 188–191 (2017). https://doi.org/10.1016/j.matlet.2017.03.050
48. G. Li, Y. Li, J. Chen, P. Zhao, D. Li, Y. Dong, L. Zhang, Synthesis and research of egg shell-yolk NiO/C porous composites as lithium-ion battery anode material. Electrochim. Acta **245**, 941–948 (2017). https://doi.org/10.1016/j.electacta.2017.06.039
49. F. Zheng, Z. Yin, H. Xia, G. Bai, Y. Zhang, Porous MnO@C nanocomposite derived from metal-organic frameworks as anode materials for long-life lithium-ion batteries. Chem. Eng. J. **327**, 474–480 (2017). https://doi.org/10.1016/j.cej.2017.06.097
50. W. Wei, S. Yang, H. Zhou, I. Lieberwirth, X. Feng, K. Mullen, 3D graphene foams cross-linked with pre-encapsulated Fe_3O_4 nanospheres for enhanced lithium storage. Adv. Mater. **25**(21), 2909–2914 (2013). https://doi.org/10.1002/adma.201300445
51. A. Ponrouch, M.R. Palacín, Optimisation of performance through electrode formulation in conversion materials for lithium ion batteries: Co_3O_4 as a case example. J. Power Sources **212**, 233–246 (2012). https://doi.org/10.1016/j.jpowsour.2012.04.005